Auto-registration and Orthorecification Algorithm for the Time Series HJ-1A/B CCD Images

BIAN Jin-hu[1,2], LI Ai-nong[1]*, JIN Hua-an[1], LEI Guang-bin[1,2], HUANG Cheng-quan[3], LI Meng-xue[3]

1 Digital Mountain and Remote Sensing Application Center, Institute of Mountain Hazards and Environment, Chinese Academy of Sciences, Chengdu 610041, China

2 University of Chinese Academy of Sciences, Beijing 100049, China

3 Department of Geography, University of Maryland, 2181 LeFrak Hall, College Park, MD 20742, United States

Corresponding author, e-mail: ainongli@imde.ac.cn; First author, e-mail: bianjinhu@imde.ac.cn

Abstract: How to deal with geometric distortion is an open problem when using the massive amount of satellite images at a national or global scale, especially for multi-temporal image analysis. In this paper, an algorithm is proposed to automatically rectify the geometric distortion of time-series CCD multi-spectral data of small constellation for environmental and disaster mitigation (HJ-1A/B) which was launched by China in 2008. In this algorithm, the area-based matching method was used to automatically search tie points firstly, and then the polynomial function was introduced to correct the systematic errors caused by the satellite motion along the roll, pitch and yaw direction. The improved orthorectification method was finally used to correct pixel displacement caused by off-nadir viewing of topography, which are random errors in the images and cannot be corrected by the polynomial equation. Nine scenes of level 2 HJ CCD images from one path/row were taken as the warp images to test the algorithm. The test result showed that the overall accuracy of the proposed algorithm was within 2 pixels (the average residuals were 37.8 m, and standard deviations were 19.8 m). The accuracies of 45.96% validation points (VPs) were within 1 pixel and 90.33% VPs were within 2 pixels. The discussion showed that three main factors including the distortion patterns of HJ CCD images, percent of cloud cover and the varying altitude of the satellite orbit may affect the search of tie points and the accuracy of results. Although the influence of varying altitude of the satellite orbits is less than the other factors, it is noted that detailed satellite altitude information should be given in the future to get a more precise result. The proposed algorithm should be an efficient tool for the geo-correction of HJ CCD multi-spectral images.

Keywords: HJ time series images; Auto-geocorrection; Topographic correction; Wide coverage CCD cameras

Introduction

Precise images co-registration is a prerequisite in many remote sensing applications such as multi-temporal classification (Li et al. 2012a), multi-sensorial data fusion (McAlpinand Meyer 2012), change detection (Huang et al. 2009), building extraction (Li et al. 2011), and canopy modeling (Li et al. 2012b; Selkowitz et al. 2012). However, the geometric distortion is often major source of limitation (Townshend et al. 1992; Bryant et al. 2003). It is time-consuming work when selecting the ground control points manually for image registration with magnanimity remote sensing images, especially in the mountainous area. To improve the geometrical accuracy and processing efficiency, more attention has been paid to the development of automatic algorithms.

Several methods concerning the automatic registration of remote sensing images have been proposed in recent years (Leprince et al. 2007;

Aguilar et al. 2008; Gao et al. 2009). Generally, it can be divided into image feature-based method and area-based matching method (Kennedy and Cohen 2003; Li et al. 2006; Wong and Clausi 2010). Feature-based methods match tie points based on features extracted from the base and warp images. These features include invariant moments (Dai and Khorram 1999), shape characteristics (Ali and Clausi 2002), contours (Li et al. 1995; Eugenio et al. 2002), and intensity gradients (Fan et al. 2007). The number of common elements in the detected sets for features should be sufficiently high, regardless of the image geometry change, radiometric conditions and changes in the scanned scenes. However, it may not be satisfied in areas with significant landscape changes. In contrast, compared the grayscale values of batches of warp and base images, area-based methods try to find conjugate image locations based on similarity in those gray scale value patterns. Through the aforementioned studies, it is evident that the area-based method is reliable for matching multi-temporal datasets (Mao et al. 2001; Bunting et al. 2008; Gao et al. 2009).

Owing to the diversity of images to be registered and various types of degradations, it is impossible to design a universal method applicable to all registration tasks (Cui et al. 2012). Launched in September 2008, the small constellation for environmental and disaster mitigation (HJ-1A/B) were developed for mitigation of the frequent natural disasters and monitor of eco-environment in China. It has been widely applied for monitoring the natural disasters and evaluating the health condition of eco-environment because of the high spatio-temporal resolution and wide field of view (FOV) (Chen et al. 2010; Chen et al. 2011; Zhao et al. 2011). However, incorrect geolocation caused by the satellite motion along the roll, pitch, yaw direction and the pixel displacement caused by the topographical variations at the off-nadir viewing angle are the bottlenecks when using the massive amount of HJ data at the national or global scale.

In this paper, we present an auto-registration and orthorectification algorithm for the HJ image processing. It uses the area-based matching algorithm to automatically search tie points and fits the coefficients of the polynomial function firstly, and then corrects the pixel displacement caused by the topographical variations at the off-nadir viewing according to the analysis of the HJ CCD imaging mechanism. To validate the accuracy of the corrected results, validation points (VPs) are automatically searched and divided into 4 sub-regions to validate the accuracy of each region. The proposed algorithm has been tested on the HJ image processing.

1 Study Region and Data Acquisition

1.1 Study region

The study area is located in the southwestern China, where is the typical alpine and gogre area (Figure 1a). It shows the HengDuan Mountain and the east of Qing-Tibet Plateau. The altitude of this study region is from 455 m to 6,225 m, and the mountainous area with slope greater than 15 degrees accounts for 75% of the whole image.
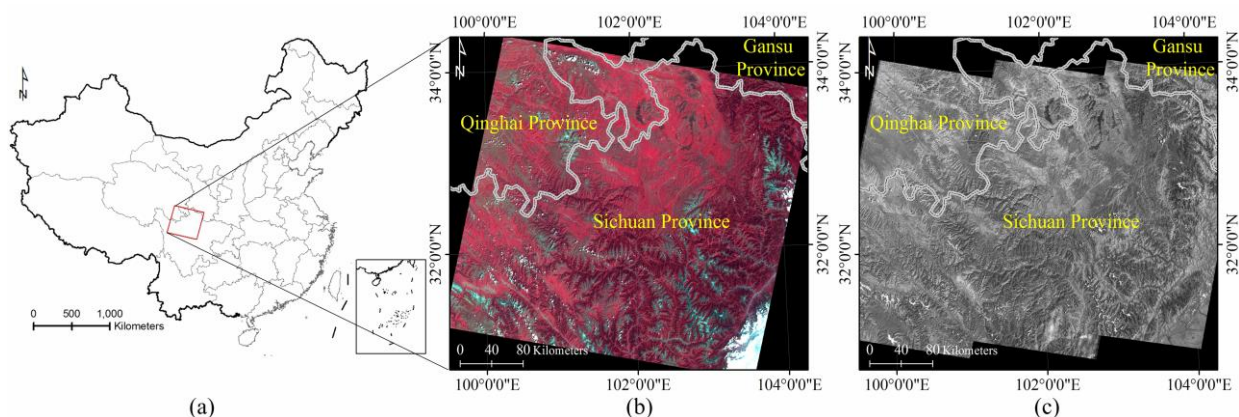
Figure 1 The base and warp images for the study region. (a) is the location of base and warp images, (b) is the CCD1 image on HJ1B of path17 row 76 acquired on August 31, 2009, (c) is the mosaic result of the near-infrared TM images.

Figure 1b is the CCD1 image of HJ1B acquired on August 31, 2009, and Figure 1c is the base image which is mosaicked by the near-infrared band of 6 scenes of TM images listed in Table 1.

1.2 Data acquisition

Three types of satellite data are used in this study. The HJ multi-spectral CCD images are the warp images. TM and the elevation data from the Shuttle Radar Topography Mission (SRTM) are the base and auxiliary DEM data.

1.2.1 HJ images

The HJ constellation consists of two small optical remote sensing satellites (HJ-1A/B) and a microwave satellite (HJ -1C). The data are gathered and distributed from the China Center for Resource Satellite Data and Application (CRESDA). Nine scenes of level 2 HJ-1A/B CCD multi-spectral images with 4 bands are taken as the warp images, which have implemented the radiometric

correction and systematic geometric correction (Table 1).

Different from Landsat TM, two wide coverage multi-spectral CCD cameras with 360 km designed swath width and 30 degree angle are loaded on the HJ-1A/B satellites. It implies that the pointing angle of each camera is 15 degree (Cao et al. 2003; Jia et al. 2009). The CCD cameras include four bands, i.e., blue (0.43-0.52 μm), green (0.52-0.60 μm), red (0.63-0.69 μm), near infrared (0.76-0.90 μm), and the spatial resolution are 30m. The data acquisition capability of HJ is stronger than most of the earth resource satellites such as TM and SPOT because of the 4 day revisit period for one satellite and 2 day after the constellation network.

Figure 2a depicts the conformation characters of CCD1 and CCD2 while the satellite descending passes. Images of CCD1 and CCD2 share the same nadir tracking line when both of them are acquired simultaneously. Along the nadir tracking line, CCD1 is on the right hand and CCD2 is on the left hand. The geometric distortion is the minimum at

Table 1 Acquiring date and the path/row for the warp and base images

No.	HJ Path/Row-Date	TM WRS-2 Path/Row-Date
1	HJ1B-CCD1-17-76-20090831-L20000164439	130/037-19940626
2	HJ1B-CCD1-17-76-20100118-L20000237758	130/038-19940626
3	HJ1B-CCD2-17-76-20100206-L20000247950	131/037-20070925
4	HJ1B-CCD2-17-76-20100313-L20000270729	131/038-19940905
5	HJ1A-CCD1-17-76-20100517-L20000310379	132/037-20050910
6	HJ1B-CCD2-17-76-20110525-L20000543637	132/038-19941014
7	HJ1B-CCD2-17-76-20100816-L20000376039	
8	HJ1B-CCD1-17-76-20101204-L20000437992	
9	HJ1B-CCD2-17-76-20101223-L20000449611	

(a)   (b)
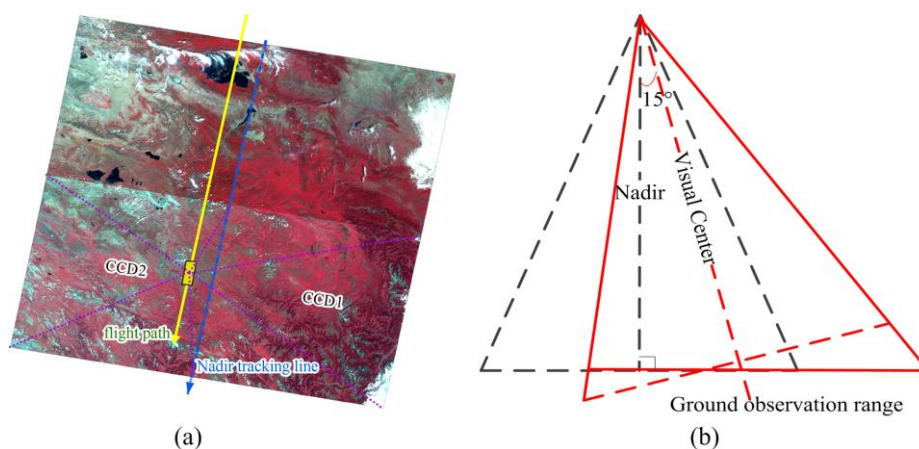
Figure 2 Conformation character of CCD camera on HJ-1A/B. Between them, (a) is the descending pass HJ images including the path and row of 17/72-CCD1, 22/72-CCD2, 17/76-CCD1 and 12/76-CCD2, which were acquired on August 31, 2009; (b) monitoring of the side viewing of CCD camera on HJ-1A/B.

the nadir viewing and increased from left to right of CCD1, while CCD2 is opposite. In order to rectify the geometric distortion, the serial number of CCD camera and the orientation of the satellite (descending or ascending passes) needs to be affirmed to analyze the regularity of the geolocation error distribution. It is noted that the visual center of HJ-1A/B is different from the TM images for the side viewing (Figure 2b). Both serial number of CCD camera and location of visual center can be obtained from the header file.

1.2.2 TM images

Landsat TM images, which have already been precisely rectified, are downloaded from the GLCF (http://glcf. umiacs.umd.edu) or USGS (http://landsat7. usgs.gov) Landsat archive and are used as the base images. Since some images in these datasets still exist large geolocation error, two criteria are set to choose the best base images, which are the cloud cover less than 5% and the geolocation error less than 0.5 pixels. Because swath of HJ is wider than TM, TM images are mosaicked into one larger base image to corresponding with the cover of HJ images. As shown in Table 1 and Figure 1b, six scenes of TM images with cloud cover less than 5% and geolocation error less than 50 m (Tucker et al. 2004) are chosen. For the area-based matching method compares the gray scale values of patches in warp and base images and tries to find conjugate image locations based on similarity in those gray scale value patterns, the near-infrared bands of TM and HJ with less atmospheric contamination are chosen as the matching band.

1.2.3 Auxiliary data

In this paper, SRTM with a spatial resolution of 90 m and WRS-2 tiles are used as base DEM data to approximate Landsat scenes. As the coverage of HJ images is wider than the tiles of SRTM, SRTM is firstly mosaicked to match with the HJ area.

All of the data sources are transformed to the UTM projection. Because the warp images may have different UTM zone numbers, the GCTP
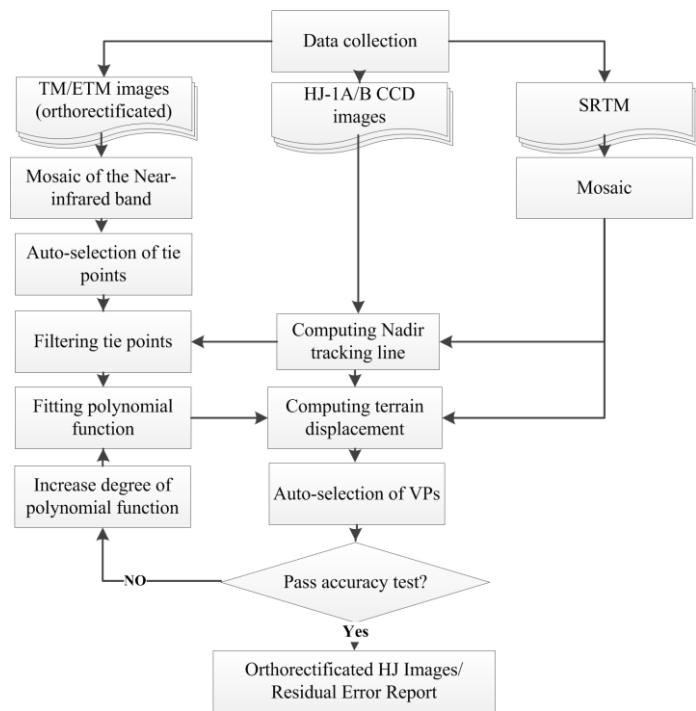
Figure 3 Flowchart for the auto-registration and orthorectification

(General Cartographic Transformation Package) (Elassal 1987) was embedded in this study to automatically transform different UTM zones for the base and warp images.

2 Algorithm Development

The overall approach is algorithmically divided into three parts: the automatic image registration, the orthorectification and accuracy validation part. The flow chart of the overall procedure is shown in Figure 3. Checking the similarity between HJ and TM images, an area-based matching method is adpoted to automatically search tie points. The pixel displacement caused by the off-nadir viewing is then corrected according to the nadir tracking line and altitude. Then, VPs are searched between the base and corrected results to validate the accuracy.

2.1 Automatic image registration

The area-based image matching approach is adopted to design the automatic image registration algorithm for HJ CCD images. In the area-based

matching procedure, a clip window (*A*) is fixed around the tie point in base image, and then the clip window (*cs*, The default value is 11 pixels) is moving on warp image (*B*) within a maximum search distance (*ms*) (The default value is 50 pixels). Point with the maximum correlation within the search distance is the tie point when it satisfies the threshold, which are the limitation of the total points (The default value is 3) and the threshold for correlation coefficient (The default value is 0.75) set before the searching procedure. The cross-correlation of the central pixel *(m, n)* between two images can be computed as:

$$R_{mn} = \frac{\sum_{i=m-cs/2}^{m+cs/2} \sum_{j=n-cs/2}^{n+cs/2} (A_{ij} - \bar{A})(B_{ij} - \bar{B})}{\sqrt{(\sum_{i=m-cs/2}^{m+cs/2} \sum_{j=n-cs/2}^{n+cs/2} (A_{ij} - \bar{A})^2)(\sum_{i=m-cs/2}^{m+cs/2} \sum_{j=n-cs/2}^{n+cs/2} (B_{ij} - \bar{B})^2)}}$$

(1)

where R_{mn} is the cross-correction coefficient of the moving windows.

Since the base images have been registered and orthorectified, tie points on the base images should be projected into the warp images and pixel displacement caused by off-nadir viewing of topography should be added up to match with the warp images. The computing method for the off-nadir viewing topography will be mentioned in Section 2.2.

After the automatic tie points searching procedure, the polynomial equation is used to correct the pixel distortions caused by the satellite motion along the roll, pitch and yaw direction, which usually are seemed as the systematic errors in the remote sensing process. Polynomial warping is available from the 1st to nth degree. Because of the usual few internal distortions in the remote sensing images, a first-degree polynomial warp is firstly conducted. A higher order polynomial function will be then adopted if the Root Mean Square (RMS) of the results cannot satisfy the accuracy according to the iteration procedure.

Iteration procedure is adopted to remove the bad tie points according to the following three criteria: (1) The RMS of the polynomial function fitted by the tie points cannot be greater than 0.75, otherwise the points with maximum prediction error are removed and coefficient of the polynomial function is fitted again. (2) Points with the prediction error more than 1 pixel are removed. (3)

The order of the polynomial function is increased if the correction error cannot satisfy the accuracy after the registration and orthorectification and the criteria 1 and 2 are repeated.

2.2 The Orthorectification algorithm for HJ

2.2.1 Orthorectification for TM

The orthorectification is used to correct pixel displacement caused by off-nadir viewing of topography, which are random errors in the images and cannot be corrected by the polynomial function. A terrain correction algorithm was developed by the Landsat 7 Image Assessment System (IAS) which analyzes the satellite nadir track line from the image to correct terrain relief displacement in TM images (J. Storey et al. 2006). In the IAS, a linear fitting function is firstly built to fit the satellite nadir tracking line using a least square fitting approach. The slope of the linear fitting function is computed by scanning the image to find valid image edge, and the intercept of the fitting equation is computed from the scenic center of the image. Once the nadir tracking line is fitted, displacement of each pixel caused by the off-nadir viewing of terrain can be calculated from the distance to the nadir tracking line and the altitude of the pixel (Steinwand and Wivell. 1993). The parameters can be given as follows:

$$S = pixel\_size \times off\_nadir\_pixel \tag{2}$$

$$s = S / Re \tag{3}$$

$$LOS = sqrt \begin{pmatrix} Re^2 + (Re + Alt)^2 - 2 \times \\ Re(Re + Alt) \times \cos(s) \end{pmatrix} \tag{4}$$

$$d = a\sin(Re \times \sin(s) / LOS) \tag{5}$$

$$dd = a\tan \begin{cases} (Re + Alt) \times \sin(d) \times (1 - (Re + \\ h) / Re) / [(Re + h) \times sqrt(1 - \\ (Re + Alt)^2 \times \sin^2(d)) / Re^2) - \\ (Re + Alt) \times \cos(d)] \end{cases} \tag{6}$$

$$z'' = a\sin[(Re + Alt) \times \sin(d + dd) / Re] \tag{7}$$

$$ds = z'' - s - (d + dd) \tag{8}$$

$$dS = Re \times ds \tag{9}$$

$$terrain\_offset = dS / pixel\_size \tag{10}$$

where *S* is the distance from pixel to the nadir tracking line, *pixel_size* stands for the nominal pixel size in meters, *Re* is the radius of the earth

reference ellipsoid at the scene center latitude, and *Alt* is the altitude of the satellite above the ellipsoid. The approaches on how to obtain these parameters can be seen in the reference paper (Storey et al. 2006).

2.2.2 Improvement of the orthorectification procedure for HJ

How to improve the accuracy of the nadir tacking line is a major concern in the IAS algorithm. Using the image coordinate system, the nadir tracking line can be expressed as:

$$ai + bj + c = 0 \qquad (11)$$

where *i* and *j* are the row and column index respectively.

However, for 2 side viewing CCD cameras on HJ-1A/B, the IAS terrain correction algorithm cannot be directly used for the correction of HJ, and needs to be improved according to the conformation character of the HJ CCD camera. As mentioned in Section 1.2.1, the nadir tackling line for HJ CCD needs to be calculated according to the pointing angle and the visual center of the image (Figure 2b). It can be fitted by a linear function using the point-slope form. The slope of the linear equation is obtained by scanning the image edge, and the point (*wcx, wcy*) can be computed as follows (Figure 4):

$$dis = Alt \times \tan\theta \qquad (12)$$

$$\begin{cases} \Delta x = dis \times \sin\alpha \\ \Delta y = dis \times \cos\alpha \end{cases} \qquad (13)$$

$$\begin{cases} wcx = cx\text{-}\Delta x \\ wcy = cy\text{-}\Delta y \end{cases} \qquad (14)$$

where *dis* is the distance from pixel to nadir, *Alt* is the altitude of the satellite, θ is the pointing angle that is 15 degrees for CCD1 and -15 degrees for CCD2 when the satellite passes descending, α is the slope of the nadir fitting function, Δx and Δy are the bias of the visual center coordinate, *cx* and *cy* are the coordinate of the visual center which can be get from the header file, *wcx* and *wcy* are the corresponding coordinates of visual center used to compute the coefficients of the linear fitting function according to the point-slope form.

2.3 Accuracy validation

In this paper, iteration procedure is adopted to verify the accuracy of orthorectified results. Validation points (VPs) are automatically searched and grouped into four sub-regions after the whole correction procedure. The orthorectified results are output only when the accuracy of over 60% VPs is less than 2 pixels in each sub-region. Otherwise, the order of the polynomial function will be increased and the geocorrection and orthorectification procedure will be repeated (Figure 3). The default set of iteration time is 2 times. When the accuracy reaches the predefined threshold (2 pixels), the final orthorectification results and the residual error report will be given.
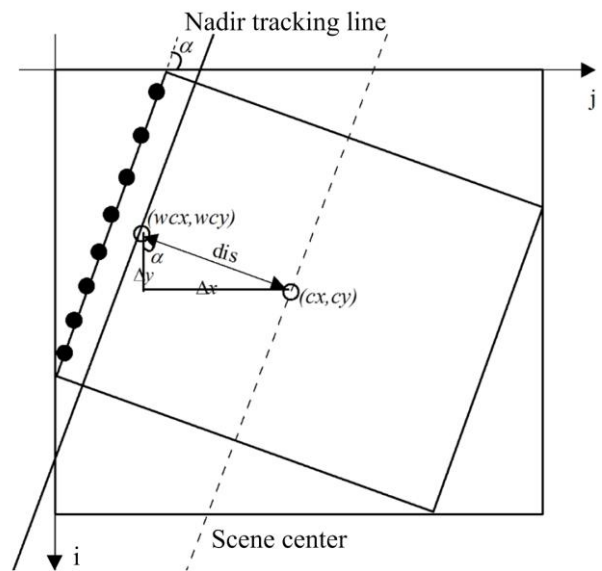
Figure 4 The calculation method for nadir tracking line of HJ

3 Results and Analysis

3.1 Visual analysis

Figure 5 depicts a visual comparison before and after geometric distortion correction for the images of HJ1B CCD1 (path 17 row 76) acquired on August 31, 2009. It is a descending pass image recorded in the header file. According to the visual center and the detecting of image edge, the linear equation for the nadir tracking line of this image is i = -4.6368j + 18231, which uses the image

coordinate system. To compare the geometric distortions and orthorectified results, three distinct regions with 200 × 200 pixels are shown for contrast. Mean distance to the nadir and the altitude of the three regions are calculated for quantitative assessment of the distortions.

The original images of HJ are shown in the left column, and the orthorectified results are shown in the middle column for visual distinction. The base images of TM are given in the right column. In the demonstration, pixel displacement in area A is few and the distortion is not obvious because of the short distance to nadir. The distance to nadir in area A is 69 km and the mean altitude is 3,912 m. According to the equations from (2) to (10), the terrain offset reaches to 391.5 m which is nearly 13 HJ pixels. Located in the right hand of the image center, area B is 240 km far away from nadir and the mean and maximum altitude of this area are 4,285 m and 4,589 m respectively. The maximum distortion of this area reaches 1,562 m which is

almost 50 pixels. The mountain body has been evidently distorted by the off-nadir viewing of topography and has been fully corrected after registration and orthorectification. On the left image boundary, area C is 348 km from nadir, and pixels in the area are distorted most serious. The northwestern slope in this area is greatly stretched and the northeastern slope is sharply compressed. The mean and maximum altitudes in this area are 3,039 m and 3,583 m respectively, and the maximum distortion of this area reaches 1,768 m, which is approximately 59 pixels. Comparing with the base images, the orthorectified results are consistent with the actual situation.

3.2 Accuracy validation

Using the image to image and stratified random sampling method, one hundred VPs are first manually selected on the warp image and orthorecification results to validate the accuracy of
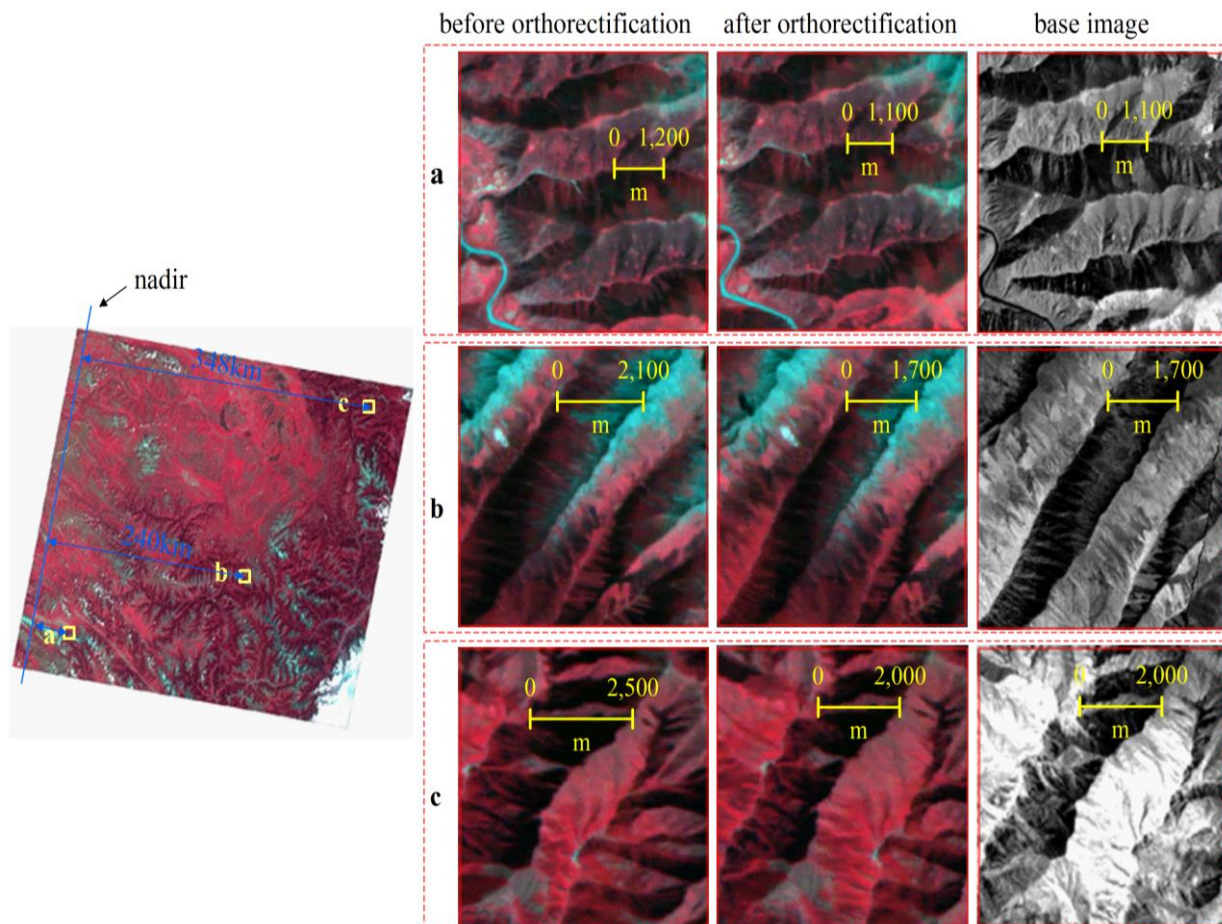
**Figure 5** Comparison of three regional areas before and after correction
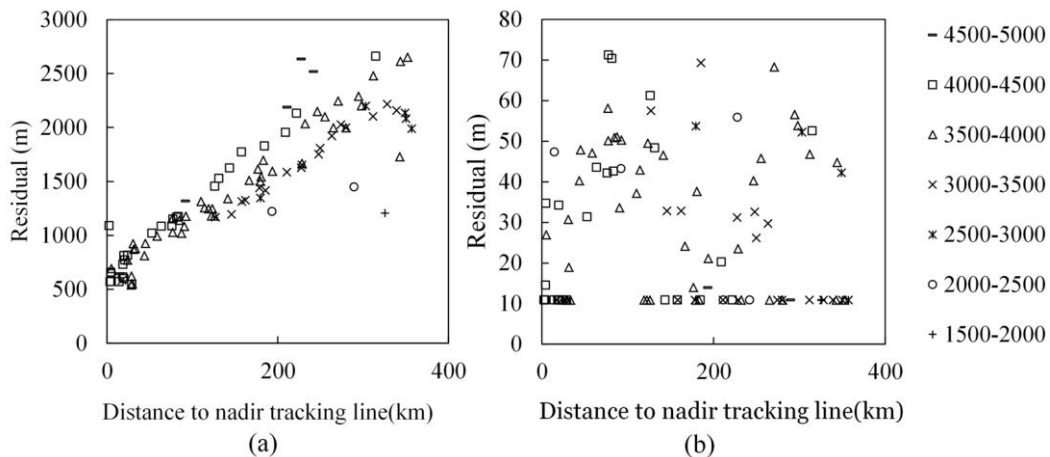
Figure 6 Scatter plots of the two dimensional residuals in 100 VPs depending on the distance to the nadir tracking line, (a) before registration, (b) after registration.

the results (Figure 6). The altitude of VPs is extracted from the SRTM data and the distance to the nadir tracking line of VPs is computed from the distance equation for point to the straight line.

The VPs are divided into 7 groups at 500 m altitude intervals. As shown in Figure 6, residual errors of VPs are highly related to the distance to nadir tracking line and linearly increase in the warp image, while the errors are independent of the distance to nadir in the orthorectified results. The correlation coefficients between residuals and distance to nadir before and after registration are 0.90 and -0.02. It indicates that the systematic errors have been successfully eliminated in the orthorectified results. In addition, residuals are correspondingly related to altitude. The correlations between residuals and altitude before and after registration are 0.16 and 0.07, which implies that topographic distortions have been successfully eliminated. It is noted that the geometric distortion of one pixel is determined both by the distance from pixel to nadir and the altitude. In Figure 6a, although the distance from pixel to nadir of some VPs is larger than others, the geolocation error is small for the lower altitude. The average residual is 1,437.63 m and the standard variance is 581.11 m in the warp images. As a result, the geolocation errors are greatly reduced. Accuracies of 55% VPs are less than one pixel and of 95% VPs are less than two pixels.

It is a time-consuming and impractical work to manually validate the accuracy of the massive amount of HJ images. This paper considers the area-based matching algorithm to automatically search the VPs between the results and the base images in the final output procedure. Figure 7 shows the error histogram for all of the VPs in the 9 HJ CCD images in Table 1. The average residuals of these images are 37.86 m and the standard error is 19.83 m. Accuracies of 45.96% VPs are within one-pixel and of 90.33% VPs are within two-pixels.
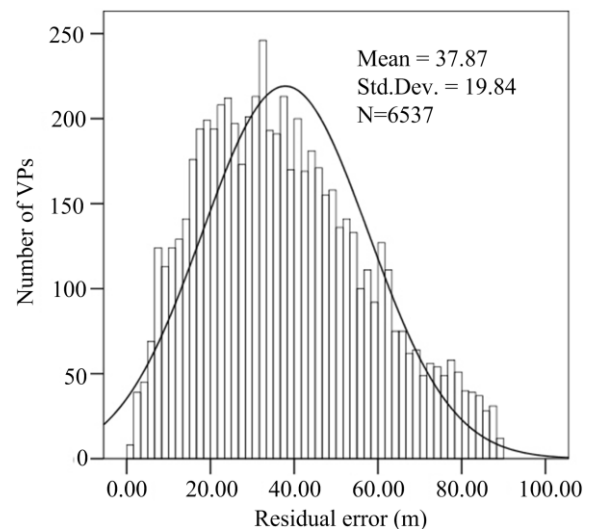
Figure 7 Histogram of the VPs for the 9 warp images

3.3 Spatial error distributions

A spatial distribution map of error contributes significantly to deepen understanding for the accurate analysis. Spatial interpolation is used to estimate the missing data according to interpolate attribute of discrete validation points. We used the

spatial Kriging interpolation method to interpolate the residuals of 100 VPs for HJ1B-CCD1-20090831.

Figure 8a presents the spatial error distribution in the warp image. On the whole, the geolocation error is from 540 to 2,657 m and gradually increases from left to right before registration. After registration and orthorectification, the residuals are within 100m and distributed uniformly.

Table 2 shows the correlation coefficients between residuals and distance to nadir/altitude of the VPs automatically searched in the 9 images after geometric corrections. The number of images in the first column in Table 2 is corresponding with the number of images in Table 1. In Table 2, the correlation coefficients between distance from pixel to nadir and altitude of each VPs are less than 0.3. It indicates that relationships between residuals

and distance to nadir or residuals and altitude does not exist anymore. The systematic and random errors in the warp images have already been eliminated. For the 9 test images, the residuals are lower than 60 m, which are about 2 pixels.

4 Discussions

4.1 The distortion patterns of HJ

According to the character analysis of HJ images, the geolocation errors for different altitude and distance from pixel to the nadir view conditions are simulated through equations from (2) to (10) and shown in Figure 9.

As shown in Figure 9, the geolocation error regularly increases with the distance to nadir under
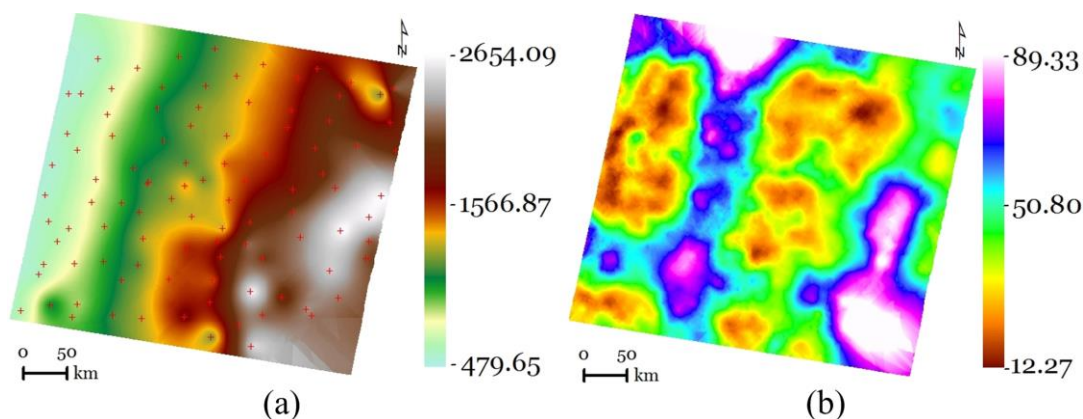
Figure 8 Spatial error distributions for the HJ1B-CCD1-20090831. The red crosses in (a) are the manually selected VPs. (a) before registration, (b) after registration.

Table 2 Correlation between altitude/distance from pixel to nadir and the residual error of VPs after geometric correction

Image No.	Correlation coefficient [a]	Correlation coefficient [b]	Residuals	Std. Dev	Validation results (VPs passed test/VPs in total)				
					Total	UL	UR	LL	LR
1	-0.02	-0.09	36.3	19.1	1634/1802	794/831	270/300	411/488	159/183
2	-0.05	0.11	41.9	22.3	201/430	80/192	11/80	103/132	7/26
3	0.12	-0.08	40.2	20.3	248/502	32/61	124/164	17/96	75/181
4	-0.07	0.21	34.7	21.4	324/522	21/42	175/218	29/63	99/199
5	0.10	0.19	39.1	25.5	437/751	110/182	187/225	83/210	57/134
6	0.18	-0.16	39.4	23.4	245/515	14/39	116/174	30/98	85/204
7	0.14	-0.15	34.1	16.9	754/1043	70/98	147/269	183/220	354/456
8	0.13	-0.11	50.3	25.1	234/529	77/225	37/104	109/147	11/53
9	0.04	0.12	39.1	21.8	251/443	41/75	122/155	36/113	52/100

Notes: [a]The correlation coefficient between VPs and distance to nadir. [b]The correlation coefficient between VPs and altitude.

the constant altitude and increases with altitude when the distance to nadir is same. According to the designed swath width mentioned in Section 1.2.1, pixel displacement can reach 1.5 km which is about 50 pixels, when the distance from pixel to nadir is 360 km and the altitude is 3 km. The geometric distortion pattern of HJ is quite different with TM images. In TM images, the visual center is in the middle image, and distance from the boundary to visual center is only around 92.5 km (the swath of TM is about 185 km). It indicates that the maximum geometric distortion in TM images approaches a quarter of HJ.

To analyze the impact of image distortion patterns in the selection of tie points, simulated nadir tracking lines are shifted from the image center to boundary by one pixel each time. Furthermore, off-nadir viewing effect for these tie points is recalculated to perform the variation tendency of the filtered tie points (Figure 10).

The linear fitting function for the image center is $i = -4.6368j + 48626$. With the shifting of the simulated nadir fitting function from the image center to left boundary, the intercept of the linear equation reduced progressively and the filtered tie points steadily increased. The valid tie points reached a maximum when the simulated nadir tracking line coincides with the actual nadir tracking line, and then gradually reduced when the simulated nadir tracking line moved from nadir to the image boundary. It is noted that the variation tendencies reveal the distortion patterns for HJ CCD images once again.

The maximum search distance will also affect searching for tie points. Since the geometric distortion is small at nadir while most serious at the image boundary, the maximum search distance should be larger than the maximum pixel displacement caused by the off-nadir viewing.
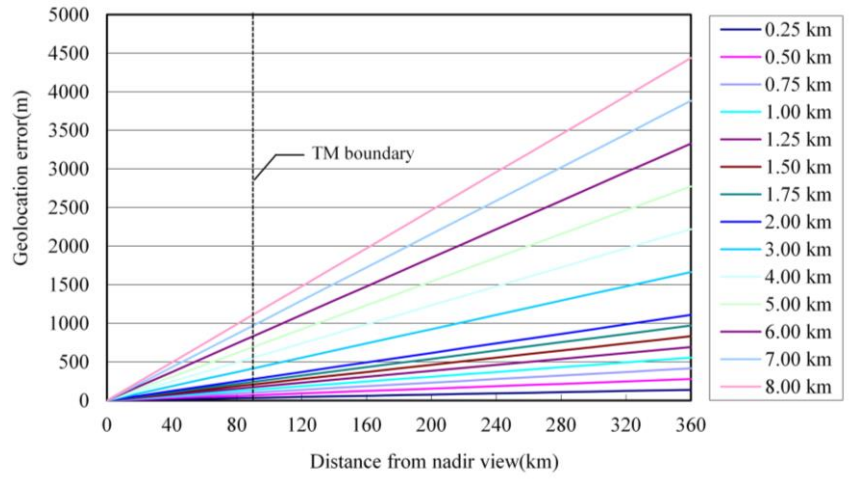

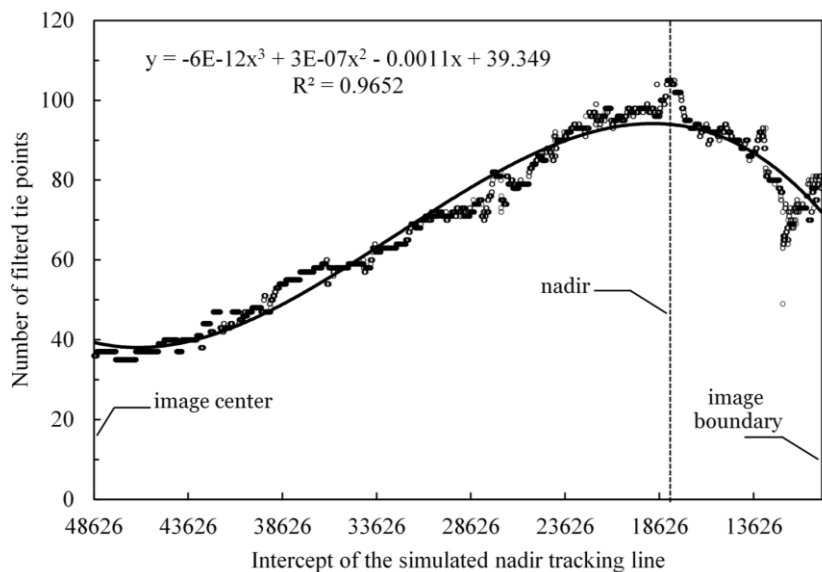**Figure 9** Theoretical analysis of terrain height incurred geolocation error

Figure 10 Variation tendencies of the filtered tie points with the simulated nadir tracking line

According to the above analysis, the pixel displacement can reach 1.5 km which is about 50 pixels when the distance from nadir view is 360 km and the altitude is 3 km. Hence, the maximum earch distance defined in this paper is 50 pixels, which can cover most terrain relief conditions.

4.2 Factors affecting the precise registration

The distribution of tie points in HJ1B-CCD1 image acquired on August 31, 2009 can be seen in Figure 11. There are 1,254 tie points in total and the distribution of tie points is relatively homogeneous. However, compared with the distribution of tie points (Figure 11a) and spatial error distribution map (Figure 8b), it can be seen that the accuracy is relatively lower in the area with no tie points than the other area, such as the white color area in Figure 8b.

As the algorithm used the area-based image matching method which based on the similarity in the gray value on base and warp images, the approximate relationship between the warp and base images is the key factor determining the correctness of the tie points and precision of the results. For the base images, more cloud cover will make it less generality. While for the warp images, too much cloud cover will make the distribution of tie points inhomogeneous and make the correction

for geometric distortion better at local and worse at the global scale. Figure 12 gives the distribution of tie points under different cloud cover conditions. While there is a little thin cloud contamination in the warp images, tie points can still be found (Figure 12a). However, the selection of tie points will be influenced when too much thick cloud is in the images (Figure 12b and Figure 12c).

4.3 Factors affecting the orthorectification

4.3.1 Spatial resolution and errors of DEM

DEM data are applied to determine the altitude of each pixel and calculate the distortion caused by the off-nadir viewing. The accuracy and spatial resolution of the DEM is the principal factors which influence the accuracy of the orthorectification results. Figure 13 gives the comparison of different DEM sources. SRTM v4.1 with standard elevation precision as ±20m and spatial resolution as 90m is chosen in this paper

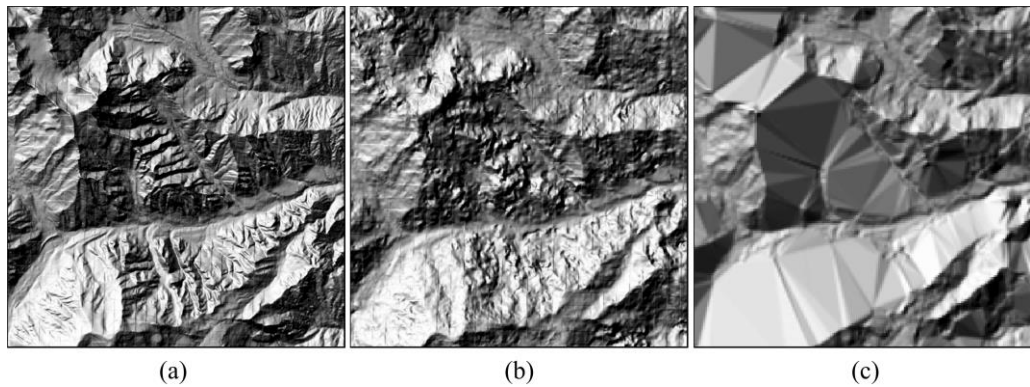| (a) | (b) | (c) |
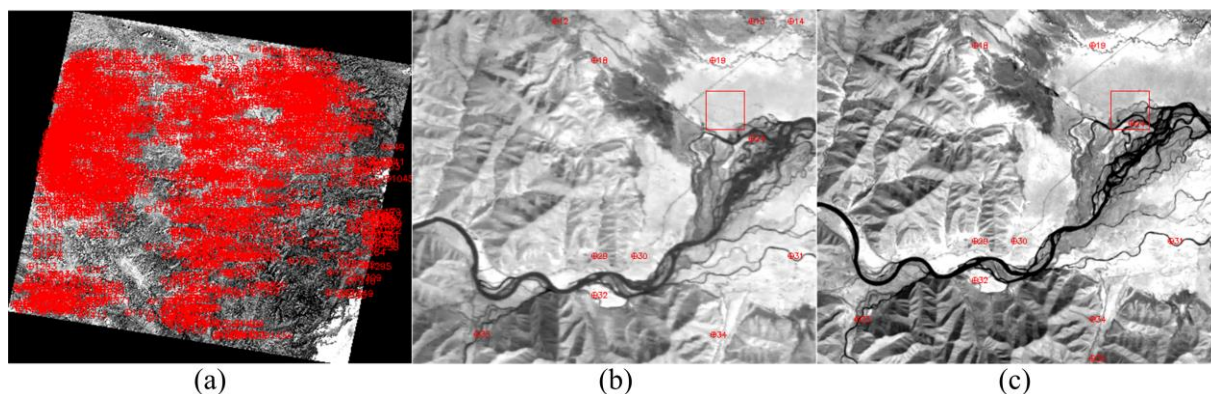
Figure 11 Distribution of the tie points. (a) the overall distribution of tie points; (b) the tie points in regional warp images; (c) the tie points in regional base images.

| (a) | (b) | (c) |
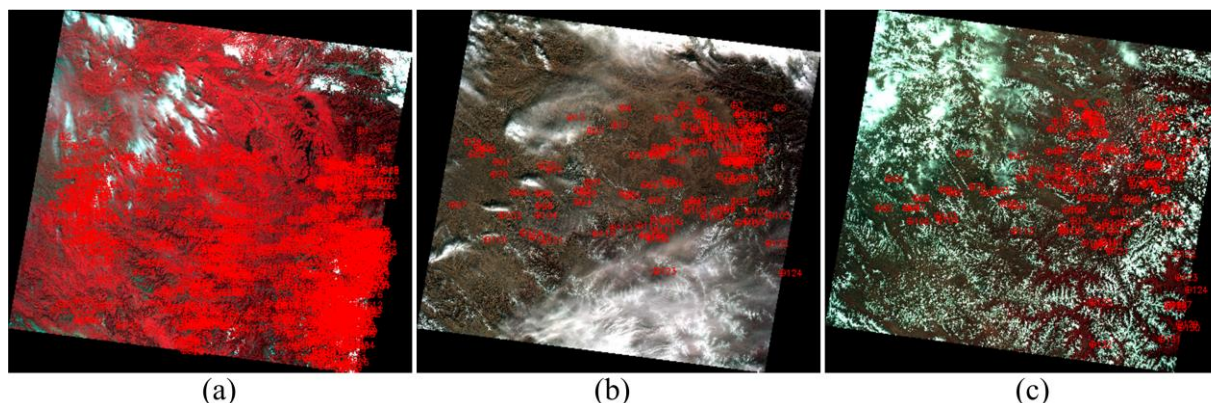
Figure 12 Distribution of tie points under different cloud cover. (a) is the distribution of tie points for HJ1B-CCD2-17-76-20100816, (b) for HJ1B-CCD2-17-76-20101223, (c) for HJ1B-CCD2-17-76-20110525.

(a)   (b)   (c)

Figure 13 Comparison of different DEM data. (a) is the hill shade generated from 1:25,000 topographic map, (b) is from ASTER GDEM, (c) is from SRTM

(Figure 13c) (Bamler 1999). Due to the radar shadow, direct reflection, phase unwrapping error or echo lag in the SRTM imaging procedure, there are some gaps in the dataset and the accuracy of these gaps rely on the accuracy of the gap-filling algorithm (Grohman et al. 2006; Luedeling et al. 2007). Compared with the DEM data generated from the 1:25,000 topographical map with a 25 m spatial resolution (Figure 13a), it can be seen that the triangular area in SRTM data cannot precisely describe the rugged topography of the mountainous area (Figure 13c). The recently released ASTER GDEM has 30 m spatial resolution and the elevation accuracy reaches 7 m. But it also has a high spatial variability in terms of accuracy which relies on the amount of overlay images. When there are fewer overlay ASTER images in some area, the accuracy will not be better than SRTM (Hirt et al. 2010; Jacobsen 2010; Hengl and Reuter. 2011). Since the ASTER GDEM is generated from the optics images, there will be some noise such as clouds or mismatch errors in the datasets (Figure 13b). Accuracy of different DEM data sources is another factor which affects the correction effects.

4.3.2 Varying altitude of the orbit of satellite

As mentioned in Section 1.2.1, the designed orbital altitude of HJ satellite is 649.093 km. However, the actual swath width of each image is unique due to the drift of the satellite. The actual measured swath width of CCD1 and CCD2 on HJ-1A is 409.849 km and 398.43 km, respectively, while the swath width of CCD1 and CCD2 on HJ-1B is 398.43 km and 401.849 km, respectively (Jia et al. 2009). Owing to no actual orbit altitude in the HJ header file, altitude of satellite orbit is set as the designed altitude minus earth radius. However, the

variation of the orbit altitude will be introduced into the orthorecification results (Leprince et al. 2007). With the increasing of orbit altitude, the geolocation error regularly increased linearly under the same altitude (Figure 14). Geolocation error will be overestimated if the actual altitude of orbit is higher than the designed altitude of orbit while underestimated if the actual altitude of orbit is lower than the designed altitude of orbit. Although the geolocation error caused by the variation of satellite orbit is less than the error caused by off-nadir viewing of topography (Geolocation error caused by variation of orbit is 41.13 m at the image boundary when the orbit is 25 km higher or lower than the designed orbit altitude), it is still necessary to provide the detailed satellite attitude data to get more accurate correcting results.
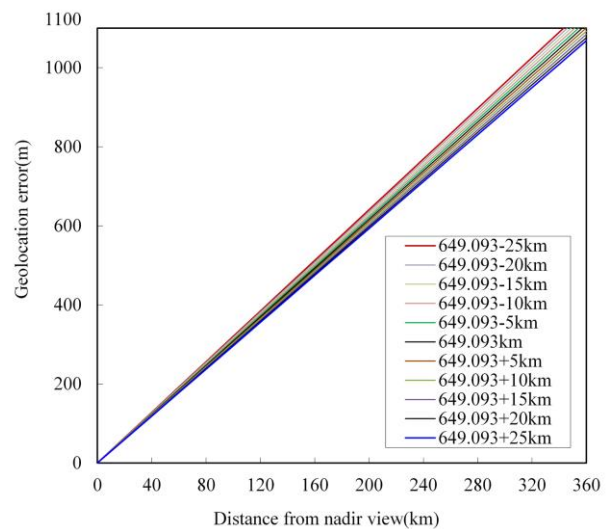
Figure 14 Theoretical analysis for variation of the satellite orbit (Altitude of terrain is 2,000 m).

5 Conclusions

The HJ CCD multi-spectral images have a large swath width and high spatio-temporal resolution, and the data acquiring capability of HJ is stronger than most satellites such as Landsat and SPOT. However, the geometric distortion in the HJ CCD images should be firstly corrected before we use them. Traditional image to image registration method selects the tie points manually and uses the polynomial function to correct the systematic errors. But in the mountainous area, due to the complexity of the rugged surface, the polynomial function cannot rectify the relief displacement caused by the off-nadir viewing. A new algorithm for the correction of geometric distortion for HJ images has been developed in this study. Based on the analysis of conformation characters of HJ CCD images, this algorithm uses the area-based method to automatically search tie points for image co-registration, and the terrain relief displacement are corrected according to the fitting of nadir tracking line, altitude of the target pixel and the distance to nadir tracking line. Accuracy assessment revealed that the geometric residual corrected by this algorithm is within 2 pixels, while visual assessment showed that most terrain displacement were corrected properly at the local area.

The proposed algorithm is an effective and high accuracy method for correcting geometric distortion in the HJ CCD images because the errors in the corrected result distributed uniformly and the algorithm is highly automatic. Accurately fitting of nadir tracking line can precisely reduce the off-nadir viewing effect of relief terrain, but it is determined by the pointing angle of the CCD camera and the varying altitude of satellite orbit. Also, the spatial resolution and residuals of DEM and the cloud distribution in images are the factors affecting the correction accuracy. The algorithm utilizes a large number of reliable tie points automatically derived through image matching. Preparing the TM base images and DEM data firstly, the batch processing has been realized for HJ CCD images, which is helpful in the processing of massive amounts of HJ CCD images.

Acknowledgements

References

Ali MA, Clausi DA (2002) Automatic registration of SAR and visible band remote sensing images. IEEE International Geoscience and Remote Sensing Symposium and 24th Canadian Symposium on Remote Sensing 1331-1333. Toronto, Canada, June, 2002. DOI: 10.1109/IGARSS.2002.1026106

Aguilar MA, Aguera F, Aguilar F J, et al. (2008) Geometric accuracy assessment of the orthorectification process from very high resolution satellite imagery for Common Agricultural Policy purposes. International journal of remote sensing 29(24): 7181-7197. DOI: 10.1080/01431160802238393

Bamler R (1999) The SRTM mission: A world-wide 30 m resolution DEM from SAR interferometry in 11 days, Heidelberg, Germany: Wichmann.

Bryant N, Zobrist A, Logan T (2003) Automatic co-registration of space-based sensors for precision change detection and analysis. IEEE International Geoscience and Remote Sensing Symposium, 1371-1373. Toulouse, France, July, 2003. DOI: 10.1109/IGARSS.2003.1294112

Bunting P, Lucas R, Labrosse F (2008) An area based technique for image-to-image registration of multi-modal remote sensing data. IEEE International Geoscience and Remote Sensing Symposium, 212–215. Boston, USA, July, 2008. DOI: 10.1109/IGARSS.2008.4780065

Cao D, Sun J, Yang B (2003) Fix and analysis of the wide coverage camera CCD. Spacecraft Recovery & Remote Sensing 24(4): 5-9. (In Chinese)

Chen J, Huan J, Hu J (2011) Mapping rice planting areas in southern China using the China Environment Satellite data. Mathematical and Computer Modelling 54(3-4): 1037-1043. DOI: 10.1016/j.mcm.2010.11.033

Chen P, Wang J, Liao X, et al. (2010) Using Data of HJ21A /B Satellite for Hulunbeier Grassland Aboveground Biomass Estimation. Journal of natural resources 25(7): 1122-1131. (In Chinese)

Cui X, Liu S, Wei X (2012) Impacts of forest changes on hydrology: a case study of large watersheds in the upper reaches of Minjiang River watershed in China. Hydrology and Earth System Sciences 16(11): 4279-4290.DOI: 10.5194/hess-16-4279-2012

Elassal AA (1987) General cartographic transformation package (GCTP), Version II. (http://www.ngs.noaa.gov/PUBS_LIB/

GeneralCartographicTransformationPackage_v2_TR_NOS12
4_CGS9.pdf, accessed on 2013-07-06)

Dai XL, Khorram S (1999) A feature-based image registration algorithm using improved chain-code representation combined with invariant moments. IEEE Transactions on Geoscience and Remote Sensing 37(5): 2351-2362. DOI: 10.1109/36.789634

Eugenio F, Marques F, Marcello J (2002) A contour-based approach to automatic and accurate registration of multitemporal and multisensor satellite imagery. IEEE International Geoscience and Remote Sensing Symposium and 24th Canadian Symposium on Remote Sensing, 3390-3392. Toronto, Canada, June, 2002. DOI: 10.1109/IGARSS.2002.1027192

Fan Y, Ding M, Liu Z, et al. (2007) Novel remote sensing image registration method based on an improved SIFT descriptor. International Symposium on Multispectral Image Processing and Pattern Recognition, International Society for Optics and Photonics. WuHan, China, November, 2007. DOI: 10.1117/12.751479

Gao F, Masek JG, Wolfe RE (2009) Automated registration and orthorectification package for Landsat and Landsat-like data processing. Journal of Applied Remote Sensing 3(1). DOI: 10.1117/1.3104620

Grohman G, Kroenung G, Strebeck J (2006) Filling SRTM voids: The delta surface fill method. Photogrammetric Engineering and Remote Sensing 72(3): 213-216.

Hengl T, Reuter H (2011) How accurate and usable is GDEM? A statistical assessment of GDEM using LiDAR data, Geomorphometry.

Hirt C, Filmer M, Featherstone W (2010) Comparison and validation of the recent freely available ASTER-GDEM ver1, SRTM ver4. 1 and GEODATA DEM-9S ver3 digital elevation models over Australia. Australian Journal of Earth Sciences 57(3): 337-347. DOI: 10.1080/08120091003677553

Huang CQ, Goward SN, Masek JG, et al. (2009) Development of time series stacks of Landsat images for reconstructing forest disturbance history. International Journal of Digital Earth 2(3): 195-218. DOI: 10.1080/17538940902801614

Storey J, Strande D, Hayes R, et al. (2006) LANDSAT 7 (L7) IMAGE ASSESSMENT SYSTEM (IAS) GEOMETRIC ALGORITHM THEORETICAL BASIS DOCUMENT (ATBD). (http://landsat.usgs.gov/documents/LS-IAS-01_Geometric_ATBD.pdf, accessed on 2013-07-06)

Jacobsen K (2010). Comparison of ASTER GDEMs with SRTM Height Models. EARSeL symposium 2010, Paris, 521-526

Jia F, Wu Y, Huang Y, et al. (2009) Technology of the wide coverage CCD carmeras for HJ-1A/1B. Spacecraft engineering 6: 37-42. (In Chinese)

Kennedy RE, Cohen WB (2003) Automated designation of tie-points for image-to-image coregistration. International Journal of Remote Sensing 24(17): 3467-3490. DOI: 10.1080/0143116021000024249

Leprince S, Barbot S, Ayoub F, et al. (2007) Automatic and Precise Orthorectification,Coregistration, and Subpixel Correlation of Satellite Images, Application to Ground Deformation Measurements. IEEE Transactions on Geoscience and Remote Sensing 45(6): 1529-1558. DOI: 10.1109/TGRS.2006.888937

Li AN, Jiang JG, Bian JH, et al. (2012) Combining the matter element model with the associated function of probability transformation for multi-source remote sensing data classification in mountainous regions. ISPRS Journal of Photogrammetry and Remote Sensing 67: 80-92. DOI: 10.1016/j.isprsjprs.2011.10.008

Li AN, Bian JH, Lei GB, et al. (2012) Estimating the Maximal Light Use Efficiency for Different Vegetation through CASA Model Combined with Time-series Remote Sensing Data and Ground Measurements. Remote sensing 4(12): 1-18. DOI: 10.3390/rs4123857

Li C, Yin J, Zhao J, et al. (2011) Extraction of urban built-up land in remote sensing images based on multi-sensor data fusion algorithms. Intelligent Computing and Information Science: 243-248. DOI: 10.1007/978-3-642-18129-0_39

Li H, Manjunath BS, Mitra SK (1995) A Contour-Based Approach to Multisensor Image Registration. IEEE Transactions on Image Processing 4(3): 320-334. DOI: 10.1109/83.366480

Li X, Zheng L, Hu Z (2006) SIFT based automatic registration of remotely-sensed imagery. Journal of remote sensing 10(6): 885-892. (In Chinese)

Luedeling E, Siebert S, Buerkert A (2007) Filling the voids in the SRTM elevation model - A TIN-based delta surface approach. ISPRS Journal of Photogrammetry and Remote Sensing 62(4): 283-294. DOI: 10.1016/j.isprsjprs.2007.05.004

Mao Z, Pan D, Huang H, et al. (2001) Automatic registration of SeaWiFS and AVHRR imagery. International Journal of Remote Sensing 22(9): 1725-1735. DOI: 10.1080/01431160118420

Michel R, Avouac JP (2002) Deformation due to the 17 August 1999 Izmit, Turkey, earthquake measured from SPOT images. Journal of Geophysical Research-Solid Earth 107(B4): 2062. DOI: 10.1029/2000JB000102

McAlpin D, Meyer F (2012) Multi-sensor data fusion for remote sensing of post-eruptive deformation and depositional features at Redoubt Volcano. Journal of Volcanology and Geothermal Research. DOI: 10.1016/j.jvolgeores.2012.08.006

Puymbroeck NV, Michel R, Binet R, et al. (2000) Measuring earthquakes from optical satellite images. Applied Optics 39(20): 3486–3494. DOI: 10.1364/AO.39.003486

Schiek C (2004) Terrain change detection using ASTER optical satellite imagery along the Kunlun fault, Tibet. M.S. thesis, Univ. Texas, El Paso, TX, 2004. [Online]. (http://www. geo.utep.edu/pub/schiek/Cara_Schiek_Master_Thesis.pdf. (Accessed on 2013-07-06)

Selkowitz DJ, Green G, Peterson B, et al. (2012) A multi-sensor lidar, multi-spectral and multi-angular approach for mapping canopy height in boreal forest regions. Remote Sensing of Environment. 121: 458-471. DOI: 10.1016/j.rse.2012.02.020

Steinwand D, Wivell C (1993) Landsat Thematic Mapper terrain coeerctions in LAS. HSTX Inter-Office Memo OAB8-21, USGS EROS Data Center, August 12, 1993.

Townshend JRG, Justice CO, Gurney C, et al. (1992) The Impact of Misregistration on Change Detection. IEEE Transactions on Geoscience and Remote Sensing 30(5): 1054-1060. DOI: 10.1109/36.175340

Tucker CJ, Grant DM, Dykstra JD (2004) NASA's global orthorectified landsat data set. Photogrammetric Engineering and Remote Sensing 70(3): 313-322.

Yu B, Yan M, Wu F, et al. (2010) The rothorectification of Ultra-Width remote sensing image. Remote sensing for land & resources 3(85): 31-35. (In Chinese)

Wong A, Clausi DA (2010) AISIR: Automated inter-sensor/inter-band satellite image registration using robust complex wavelet feature representations. Pattern recognition letters 31(10): 1160-1167. DOI: 10.1016/j.patrec.2009.05.016

Zhao S, Qin Q, Zhang F, et al. (2011) Research on Using a Mono-Window Algorithm for Land Surface Temperature Retrieval from Chinese Satellite for Environment and Natural Disaster Monitoring(HJ-1B) Data. Spectroscopy and Spectral Analysis 31(6): 1552-1556. (In Chinese)